

RESEARCH ARTICLE | JULY 19 2024

# Charge exchange recombination spectroscopy on the alkali beam of Wendelstein 7-X

Special Collection: [Proceedings of the 25th Topical Conference on High-Temperature Plasma Diagnostics](#)

B. G. Csillag ; G. Anda ; G. Cseh ; D. Dunaj; O. P. Ford ; E. Flom; D. Gradic ; F. Henke; M. Krychowiak ; D. Nagy ; M. Otte ; D. I. Réfy ; K. Tókési ; M. Vécsei ; S. Zoletnik ; the W7-X Team



*Rev. Sci. Instrum.* 95, 073524 (2024)

<https://doi.org/10.1063/5.0219461>



**APL Energy**

**Latest Articles Online!**

**Read Now**



# Charge exchange recombination spectroscopy on the alkali beam of Wendelstein 7-X

Cite as: Rev. Sci. Instrum. 95, 073524 (2024); doi: 10.1063/5.0219461

Submitted: 17 May 2024 • Accepted: 2 July 2024 •

Published Online: 19 July 2024



View Online



Export Citation



CrossMark

B. G. Csillag,<sup>1,a)</sup> G. Anda,<sup>1</sup> G. Cseh,<sup>1</sup> D. Dunai,<sup>1</sup> O. P. Ford,<sup>2</sup> E. Flom,<sup>2</sup> D. Gradic,<sup>2</sup> F. Henke,<sup>2</sup> M. Krychowiak,<sup>2</sup> D. Nagy,<sup>1</sup> M. Otte,<sup>2</sup> D. I. Réfy,<sup>1</sup> K. Tőkési,<sup>1,3</sup> M. Vécsei,<sup>2</sup> S. Zoletnik,<sup>1</sup> and the W7-X Team<sup>b)</sup>

## AFFILIATIONS

<sup>1</sup>HUN-REN Centre for Energy Research, 1121 Budapest, Hungary

<sup>2</sup>Max-Planck-Institute für Plasmaphysik, 17491 Greifswald, Germany

<sup>3</sup>HUN-REN Institute for Nuclear Research, 4026 Debrecen, Hungary

**Note:** This paper is part of the Special Topic on Proceedings of the 25th Topical Conference on High-Temperature Plasma Diagnostics.

<sup>a)</sup>Author to whom correspondence should be addressed: [csillag.barnabas@ek.hun-ren.hu](mailto:csillag.barnabas@ek.hun-ren.hu)

<sup>b)</sup>See author list of Ref. 1.

## ABSTRACT

Measurements of ion temperature profiles are required to assess the energy and particle transport processes in the Wendelstein 7-X stellarator. This device is equipped with a diagnostic alkali beam, which can be utilized to determine local impurity temperatures and densities by Charge Exchange Recombination Spectroscopy (CXRS). It could provide such profiles in the edge plasma, where other diagnostics are less efficient. With this contribution, first results of CXRS measurements on the sodium beam from the scientific operation phase OP2.1 are presented. The spectroscopic system was in commissioning phase lacking some of the final optical components. Thus, the aim of the diagnostics during this campaign was to explore the measurement capabilities. Based on the processed spectra, the prospects of  $C^{5+}$  and  $C^{6+}$  ion temperature and concentration measurements are discussed. The results indicate that with the final optical setup under installation, the diagnostics could provide ion temperature profiles in the edge with 3 mm radial resolution and at least 1 s temporal resolution.

© 2024 Author(s). All article content, except where otherwise noted, is licensed under a Creative Commons Attribution (CC BY) license (<https://creativecommons.org/licenses/by/4.0/>). <https://doi.org/10.1063/5.0219461>

## I. INTRODUCTION

Wendelstein 7-X (W7-X) is a stellarator built mainly to demonstrate neoclassical transport reduction by computational optimization of the vacuum magnetic field<sup>1,2</sup> (besides other aims as showing the feasibility of long pulse, fusion-relevant plasmas, etc.), consequently proving that the optimized stellarator concept is attractive and viable as a fusion power plant. In order to assess the performance, measurements of particle density and temperature profiles are required. For ion temperature measurements, the device is equipped with an x-ray imaging crystal spectrometer<sup>3</sup> and a Charge Exchange Recombination Spectroscopy (CXRS) diagnostics, which utilizes the heating beams<sup>4</sup> (both systems measure in the core). Ion temperatures in the Scrape-off Layer (SOL) are also determined through divertor spectroscopy.<sup>5</sup> However, these systems are not

optimal to measure local ion temperatures in the edge close to the Last Closed Flux Surface (LCFS). Consequently, a diagnostics that could provide such profiles in the edge and the SOL with high radial resolution would be of great value.

CXRS has been a widespread technique to measure local impurity temperatures in tokamak and stellarator plasmas for decades.<sup>6</sup> This method utilizes the large cross sections of charge exchange reactions between plasma impurity ions and neutral particles of an injected beam (compared to the cross sections of electron collision induced excitations in the impurities). The electrons in the impurities occupy excited states after the charge transfer, and then, they emit photons when they undergo a subsequent spontaneous transition. By measuring the Doppler shift, Doppler broadening, and intensity of these spectral lines, one can determine local impurity parameters such as velocity, temperature, and density,

respectively—assuming local thermal equilibrium. This technique is most commonly used on heating beams; however, there are examples of impurity temperature measurements utilizing high energy diagnostic lithium atoms as electron sources.<sup>7–9</sup> An advantage of such diagnostics is that lithium CX cross sections are larger by two orders of magnitude relative to protium beams;<sup>7</sup> thus, a much smaller current density is needed (a diagnostic alkali beam usually operates with a few mA/cm<sup>2</sup>). Consequently, these beams<sup>10</sup> have negligible heating effects, while their small width offers a high spatial resolution for CXRS measurements.

The present contribution examines the possibilities of CXRS measurements on the high energy sodium beam of W7-X<sup>11</sup> in order to acquire impurity temperature profiles in the boundary plasma of the device. The results of the last experiment campaign (operation phase 2.1—OP2.1) are discussed, and predictions are made for future measurements.

## II. EXPERIMENTAL SETUP

Figure 1 illustrates the experimental setup. The sodium beam is placed on the equatorial plane at  $\varphi = 72^\circ$  in cylindrical coordinates around the device.<sup>11</sup> It was operated with 50 keV atom kinetic energy in OP2.1, and the beam diameter was  $\sim 2$  cm. 150 ms periodic chopping was applied to allow for the determination of the background light. The upper port in Fig. 1 is used for  $n_e$  profile and turbulence measurements<sup>12,13</sup> by detecting the radial distribution and fluctuations in the intensity of the Na doublet line at  $\sim 589$  nm. For spectral measurements, the light is collected in the lower port,<sup>14</sup> collimated to 132 fibers, less than half of which is available to monitor the alkali beam. The spot size of the fibers on the midplane is about 2.5 mm with 0.5–1 mm distance between the spots—there are some uncertainties due to manufacturing reasons. The optical setup transmits light in the 340–930 nm wavelength range. The fibers carry the light into the spectroscopy laboratory, where it is processed by an IsoPlane SCT 320 spectrometer (from Princeton Instruments). It is equipped with a motorized, adjustable slit (5–150  $\mu\text{m}$ ), and three grids blazed at 500 nm, having 1200, 1800, and 2400 grooves/mm. A ProEM CCD camera with  $1024 \times 1024$  pixels measures the light at the output of the spectrometer.

In OP2.1, only 4 temporary fibers were installed in the laboratory with 400  $\mu\text{m}$  core diameter; however, the fibers attached to the spectrometer had 140  $\mu\text{m}$  core diameter; thus, 88% of the incoming light was lost in the couplings. The wavelength calibration of the

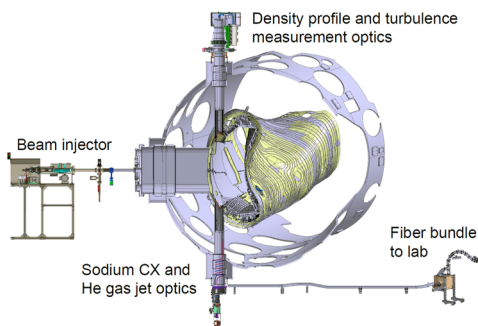


FIG. 1. Entire W7-X alkali beam diagnostic system.<sup>14</sup>

system was carried out with spectral lamps. 10–20 lines (depending on the grid) were used for such purpose. Assuming a third-order polynomial relation between the pixel and the wavelength values, the accuracy of the calibration was assessed to be 50–150 pm depending on the grid and the distance from the central wavelength setting in the spectra. In the presented measurements, 100  $\mu\text{m}$  slit width was applied to achieve a compromise between spectral resolution and light intensity, while the 1200 grooves/mm grid was equipped, since it allowed the observation of a wide wavelength range. The ProEM camera was operated with 20 ms exposure time. In data processing, the spectra measured during beam switching were dropped. The measured data were integrated in each discharge for several seconds under non-transient plasma conditions to improve the signal-to-noise ratio (SNR). The uncertainties of the intensities denoted with  $\Delta I[\lambda]$  in (7) were given by the standard deviations of the signals at individual wavelengths.

## III. THEORETICAL METHODS

The classical trajectory Monte Carlo (CTMC) method was used to determine the charge exchange cross sections for fast sodium atom and carbon ion collisions. The CTMC method is a non-perturbative method, based on the calculation of a large number of individual particle trajectories when the initial atomic states are chosen randomly.<sup>15,16</sup> One of the advantages of such method is that many-body interactions are exactly taken into account during the collisions on a classical level. In the present work, the CTMC simulations were made in a three-body approximation. In our approximation, the many-electron target atom was replaced by a one-electron atom and the projectile ion was taken into account as one particle. The three particles are characterized by their masses and charges, and the Coulomb force is acting between the colliding particles. The effective charge of the target core was calculated according to Slater's rules.<sup>17</sup> The randomly selected initial conditions were the impact parameter of the projectile with respect to the target atom, and the position and velocity vector of the target electron keep moving in Kepler orbits. The initial conditions of the individual collisions are chosen at sufficiently large inter-nuclear separations from the collision center, where the interactions among the particles are negligible. The classical equations of motion were integrated with respect to the time as an independent variable by the standard Runge–Kutta method, and the state selective charge exchange total cross sections can be calculated by

$$\sigma = \frac{2\pi b_{\max}}{T_N} \sum_j b_j^{(ion)}, \quad (1)$$

where the associated statistical uncertainty is

$$\Delta\sigma = \sigma \left[ \frac{T_N - T_N^{(ion)}}{T_N T_N^{(ion)}} \right]^{1/2}. \quad (2)$$

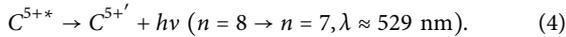
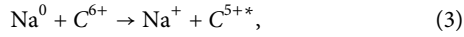
In (1) and (2),  $T_N$  is the total number of trajectories calculated for impact parameters less than  $b_{\max}$ ,  $T_N^{(ion)}$  is the number of trajectories that satisfy the criteria for state selective charge exchange, and  $b_j^{(ion)}$  is the actual impact parameter for the trajectory corresponding to the state selective CX process.

The results in Fig. 2 show that the  $n = 7$  and  $n = 8$  levels with the highest  $l$  will be occupied most likely in the  $C^{6+}$  ions, similarly to Li- $C^{6+}$  charge exchange measurements.<sup>7</sup> In the case of  $C^{5+}$  ions, the most significant population after charge transfer is expected in the  $n = 6$  and  $n = 7$ , high  $l$  levels.

## IV. RESULTS

### A. C VI line

Figure 3 shows a detected C VI line. The difference between its intensity measured with and without beam injection could be the consequence of the following reactions:



This is the most often used spectral line for hydrogen CX measurements<sup>4,6</sup> and was the strongest active line in the measured spectra. An oscillation was found with 150 ms periodicity in the temporal auto-correlation of the wavelength band of this line, which confirms that it is modulated by the beam. Furthermore, the large cross sections in Fig. 2 for  $n = 8$ , high  $l$  levels suggests that this modulation is caused by charge exchange between the beam atoms and the  $C^{6+}$  impurities, as it was stated in (3). To obtain  $T_{C^{6+}}$  from the measurements, one has to take into account the following effects:

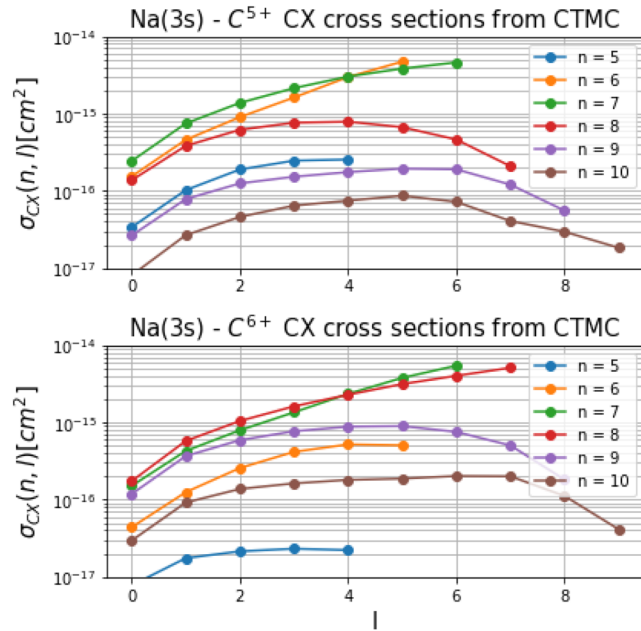


**FIG. 2.** Charge exchange cross section acquired from CTMC calculations as a function of the principal quantum number  $n$  and an azimuthal quantum number  $l$ —these denote the place of the electron after the reaction. In the simulations, sodium beam atoms with 50 keV kinetic energy were applied, which collided with  $C^{5+}$  and  $C^{6+}$  ion targets. Although the uncertainties [given by (2)] are not denoted, they were found to be always less than 10%.

20230316.072, beam on and off spectra, R = 6.2079 m, [6,12] s

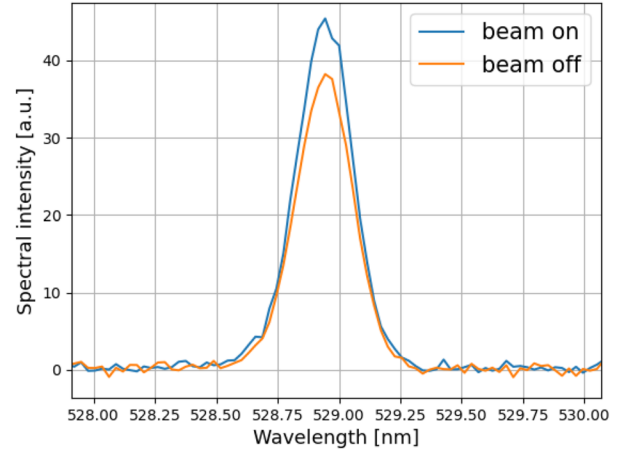


**FIG. 3.** C VI spectra measured during beam-on and beam-off periods, averaged over 6 s in the edge, at R = 6.2097 m (while the LCFS was at R  $\approx$  6.225 m—low mirror magnetic configuration).

1. The fine structure and the Zeeman splitting due to the magnetic field were calculated using the same code as in Ref. 5. One notable difference is that in this work, we process active signals, and the magnetic field vector is sufficiently known<sup>18</sup> from the intersection of the lines of sights of the channels and the beam; thus, we do not need to fit the magnetic field strength or the angle between that and the line of sight. These values are acquired from the vacuum field in the center of the measured volumes.
2. The Doppler broadening and shift (for an ideal, infinitely narrow line) results in the line shape as

$$D(\lambda; \sigma_{D,i}, I_0, \mu) = \frac{I_0}{\sqrt{\pi} \cdot \sigma_{D,i}} \cdot \exp\left[-\left(\frac{\lambda - \mu}{\sigma_{D,i}}\right)^2\right], \quad (5)$$

where  $I_0$  is a free intensity factor,  $\lambda$  denotes the wavelength, and  $\mu$  is the central wavelength of the spectral line in question, while  $\sigma_{D,i}$  is a broadening parameter, from which the ion temperature for a given species is

$$T_i = \frac{M_i}{2k_B} \left(\frac{c}{\mu}\right)^2 \cdot \sigma_{D,i}^2. \quad (6)$$

In this expression,  $M_i$  refers to the mass of the ion,  $k_B$  is the Boltzmann constant, and  $c$  is the speed of light in vacuum.  $I_0$ ,  $\sigma_{D,i}$ , and  $\mu$  are parameters to be fitted to the measured spectra.

3. The instrumental function was measured during the wavelength calibration with spectral lamps.

Figure 4 illustrates the components of C VI spectral line modeling. Thus, we can simulate a spectrum  $S(\mu, I_0, T_i)[\lambda]$  and then fit this to the measured one  $M[\lambda]$  by minimizing

$$\chi^2 = \sum_{\lambda} \frac{(S(\mu, I_0, T_i)[\lambda] - M[\lambda])^2}{\Delta I^2[\lambda]}. \quad (7)$$

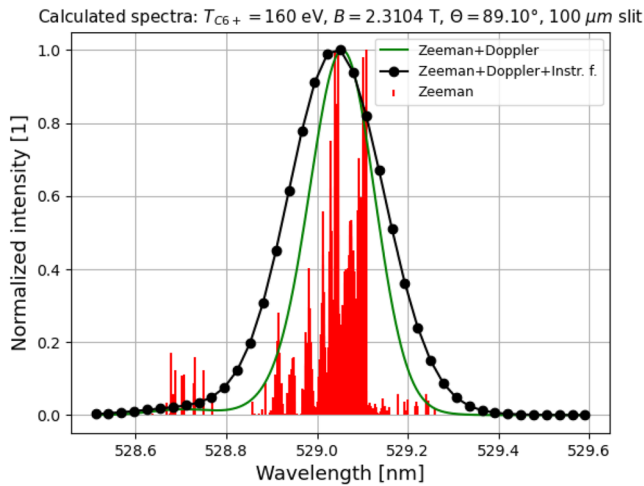


**FIG. 4.** Simulated C VI ( $n: 8 \rightarrow 7$ ) line with  $100 \mu\text{m}$  slit width and 1200 grooves/mm grid, without noise. The physical parameters were  $k_B T_{C6+} = 160 \text{ eV}$  carbon temperature,  $B = 2.3104 \text{ T}$  magnetic field strength, and  $\theta = 89.1^\circ$  angle between LOS and magnetic field.

An example of a fitted spectrum is shown in Fig. 5. The fit contains nonlinear elements; thus, the parabola approximation around the minimum value of  $\chi^2$  was not deemed sufficient for determining the uncertainty of the acquired temperature. In order to obtain that, Monte Carlo error calculations were performed. In other words, 1000 synthetic spectra were generated by sampling random noise on the fitted spectrum (red curve in Fig. 5) from a Gaussian distribution using the intensity errors  $\Delta I[\lambda]$  from the measured spectrum as sigma parameters, and then, the theoretical spectrum was fitted to the synthetic ones. This resulted in a series of  $T_{C6+}$  values, and the

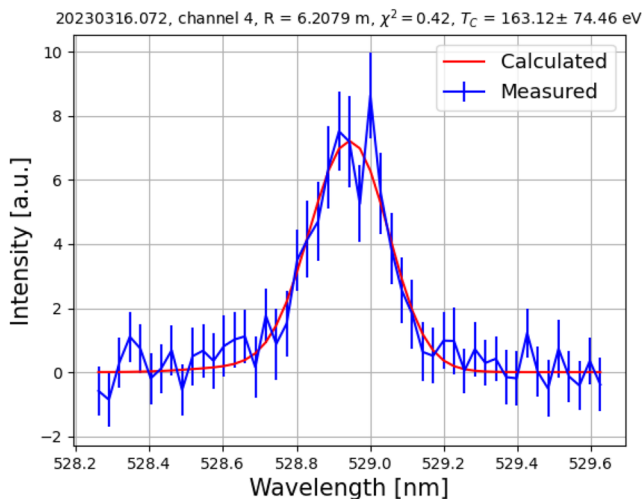


**FIG. 5.** Background subtracted C VI spectrum averaged over 6 s in the edge, at  $R = 6.2097 \text{ m}$  (while the LCFS was at  $R \approx 6.225 \text{ m}$ —low mirror magnetic configuration), and the fitted spectral model.

standard deviation of this distribution was taken as  $\Delta T_{C6+}$ . In Fig. 5, this process resulted in  $k_B T_{C6+} = 163 \pm 74 \text{ eV}$ .

In order to assess the measurement capabilities of the final system, we use a noise model where the variance of the intensity is described as  $\Delta I(I) \approx a \cdot \sqrt{I} + b$ , where the first term on the right-hand side stands for the photon statistical noise and the second term stands for the constant electronic noise of the camera. The  $a$  and  $b$  parameters were fitted using measurements of the sodium line emission during constant plasma conditions in the same spectrometer. The result is  $a = 0.0813$  and  $b = 0.4472$ . Using this method, we can sample noise for spectra with arbitrary intensities. Consequently, we can estimate the magnitude of  $\Delta T_{C6+}$  of future measurements assuming the same plasma parameters as in Fig. 5, but without signal loss in the fiber couplings (which will be the setup in OP2.2). Our projections gained in the presented manner indicate that with a 2400 grooves/mm grid and a  $100 \mu\text{m}$  slit width settings,  $\Delta T_{C6+} \approx 17 \text{ eV}$  is achievable for one second integration time in OP2.2 (assuming the same conditions as in Fig. 5). At certain radial locations, six fibers are installed in the optics; therefore, the integration time might be reduced by summing up the signals of these fibers in the spectrometer while keeping the same uncertainty level.

### B. C V line

Figure 6 shows that a spectral line at 494.5 nm was also modulated by the beam. Although the SNR on the line is smaller compared to the C VI line as shown in Fig. 3, the temporal auto-correlation of its wavelength averaged signal (just like in the case of the C VI line) confirms that the net spectral line is a result of the interactions between beam and plasma particles. While there are overlapping O V, B V, and C V CX lines at this wavelength, the dominant impurity in Wendelstein 7-X is carbon.<sup>19</sup> However, the boron density might be in the same order, or maybe even higher after boronizations, in which the carbon concentration drops. Meanwhile, the device was boronized only three weeks before the discharge in question; thus, this measured line should be mostly emitted by C V ions.

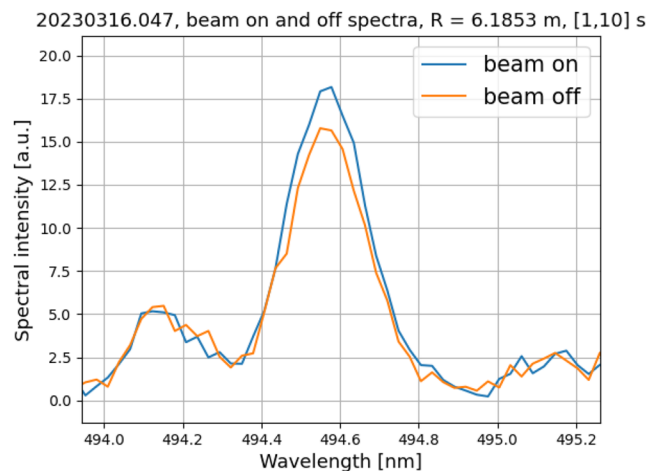


**FIG. 6.** C V spectra measured during beam-on and beam-off periods, averaged over 9 s in the edge, at  $R = 6.1853 \text{ m}$  (while the LCFS was at  $R \approx 6.202 \text{ m}$ —standard magnetic configuration).

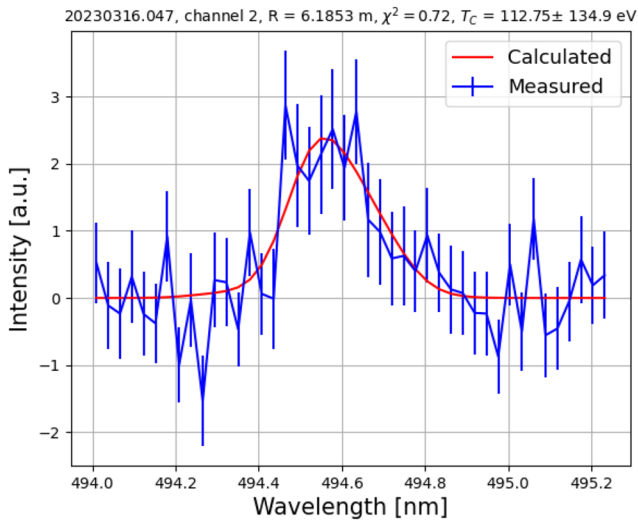
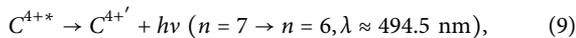
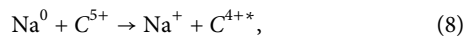


**FIG. 7.** Background subtracted C V spectra averaged over 9 s in the edge, at  $R = 6.1853$  m (while the LCFS was at  $R \approx 6.202$  m—standard magnetic configuration), and the fitting spectrum model.

Consequently, we identify the line in Fig. 6 as a C V line for now; thus, the following reactions are responsible for its modulation:



where the spectral line is emitted by the sum of a  $6h-7i$ , a  $6g-7h$ , and a  $6f-7g$  transition.<sup>8,20</sup> Furthermore, Fig. 2 suggests that the modulation on that C V line is driven by charge exchange, since the  $n = 7$ , large  $l$  levels are occupied with a high probability after such reactions.

To gain  $T_{\text{C}^{5+}}$  from the measured spectra, the same method was applied as for the C VI line. However, the Zeeman components of the line were approximated with the components of the corresponding B V line due to the absence of atomic data. Nevertheless, at this wavelength resolution, the difference between the two is expected to be small. An example of the results is shown in Fig. 7, where  $T_{\text{C}^{5+}} = 113.75 \pm 134.90$  eV. The MC error calculation method likely underestimates  $\Delta T_{\text{C}^{5+}}$  in this case since it is not possible to fit a negative temperature. We can predict the magnitude of  $\Delta T_{\text{C}^{5+}}$  for future measurements the same way as we did in the case of the C VI line. This gives a projection of  $\Delta T_{\text{C}^{5+}} \approx 37$  eV in OP2.2 with a 1800 grooves/mm grid and a  $100 \mu\text{m}$  slit width (again, assuming the same plasma conditions as in Fig. 7).

## V. UPGRADE FOR OP2.2

Sufficient fibers (with  $160 \mu\text{m}$  core diameter instead of 400) have been installed between the optics and the spectrometer since OP2.1, which allows a much better exploitation of the incoming light. Fifty-four fibers will measure the intersection of the beam and the plasma covering the SOL and the edge with 3 mm radial resolution as a result of this upgrade. Using a large number of fibers

(up to 12 in the spectrometer), it will be possible to reduce the temperature measurement uncertainty at the expense of some reduction in the spatial resolution. Although the present work focuses on the prospect of carbon temperature measurements, data processing algorithms for  $\text{C}^{5+}$  and  $\text{C}^{6+}$  density calculations are in development as well.

## VI. SUMMARY AND OUTLOOK

The presented results prove that the charge exchange cross sections between fast Na atoms and  $\text{C}^{6+}$  and  $\text{C}^{5+}$  plasma ions are sufficiently large to use the alkali beam for CXRS measurements, since C VI and C V lines were modulated by such reactions. Based on our estimations, the modulation on the C VI line should allow the measurement of  $T_{6+}$  with 10% uncertainty in the edge at 1 s temporal resolution and 3 mm radial resolution in the new experimental setup.

The picture is more complex in the case of the C V spectrum. First, there are other significant impurities in the plasma, such as oxygen and boron,<sup>19</sup> and both have charge exchange excited lines effectively at the same wavelength as the C V line: 494.5 nm. These lines were neglected in the present analysis; however, they must be taken into account when the signal is stronger. Second, as shown in Sec. IV B, this line is considerably weaker than the C VI. Thus, according to the magnitude estimations,  $\approx 33\%$  uncertainties are expected with 2 s temporal resolution and 6 mm radial resolution at best. Nevertheless, the ionization potential of  $\text{C}^{5+}$  is smaller than that of the  $\text{C}^{6+}$ ; thus, a relatively larger population is expected from the former close to the LCFS. Ion temperature data from that region would be more beneficial. Consequently, it is worth considering CXRS measurements on the C V line as well, at least in certain scenarios.

## ACKNOWLEDGMENTS

This work was carried out within the framework of the EUROfusion Consortium, funded by the European Union via the Euratom Research and Training Programme (Grant Agreement No. 101052200—EUROfusion). Views and opinions expressed are, however, those of the author(s) only and do not necessarily reflect those of the European Union or the European Commission. Neither the European Union nor the European Commission can be held responsible for them.

## AUTHOR DECLARATIONS

### Conflict of Interest

The authors have no conflicts to disclose.

### Author Contributions

**B. G. Csillag:** Conceptualization (equal); Data curation (lead); Investigation (lead); Methodology (equal); Software (equal); Visualization (lead); Writing – original draft (lead); Writing – review & editing (equal). **G. Anda:** Methodology (equal); Resources (equal); Writing – review & editing (supporting). **G. Cseh:** Resources

(equal). **D. Dunai**: Investigation (supporting); Methodology (equal). **O. P. Ford**: Conceptualization (supporting); Software (equal); Writing – review & editing (supporting). **E. Flom**: Resources (equal). **D. Gradic**: Conceptualization (supporting); Investigation (supporting); Resources (supporting); Software (equal). **F. Henke**: Resources (equal). **M. Krychowiak**: Project administration (equal); Resources (supporting). **D. Nagy**: Methodology (supporting); Resources (equal). **M. Otte**: Project administration (equal); Resources (supporting). **D. I. Réfy**: Methodology (equal); Writing – review & editing (supporting). **K. Tókési**: Resources (equal); Writing – original draft (supporting). **M. Vécsei**: Investigation (supporting); Methodology (equal); Project administration (supporting); Resources (equal); Writing – review & editing (supporting). **S. Zoletnik**: Conceptualization (equal); Funding acquisition (lead); Investigation (supporting); Methodology (equal); Project administration (equal); Resources (equal); Supervision (lead); Writing – review & editing (supporting).

## DATA AVAILABILITY

The data that support the findings of this study are available from the corresponding author upon reasonable request.

## REFERENCES

- <sup>1</sup>T. S. Pedersen *et al.*, “Experimental confirmation of efficient island divertor operation and successful neoclassical transport optimization in Wendelstein 7-X,” *Nucl. Fusion* **62**, 042022 (2022).
- <sup>2</sup>C. D. Beidler *et al.*, “Demonstration of reduced neoclassical energy transport in Wendelstein 7-X,” *Nature* **596**, 221–226 (2021).
- <sup>3</sup>N. Pablant *et al.*, “Correction and verification of x-ray imaging crystal spectrometer analysis on Wendelstein 7-X through x-ray ray tracing,” *Rev. Sci. Instrum.* **92**, 043530 (2021).
- <sup>4</sup>O. P. Ford *et al.*, “Charge exchange recombination spectroscopy at Wendelstein 7-X,” *Rev. Sci. Instrum.* **91**, 023507 (2020).
- <sup>5</sup>D. Gradic *et al.*, “Impurity temperatures measured via line shape analysis in the island scrape-off-layer of Wendelstein 7-X,” *Plasma Phys. Controlled Fusion* **64**, 075010 (2022).
- <sup>6</sup>R. C. Isler, “An overview of charge-exchange spectroscopy as a plasma diagnostic,” *Plasma Phys. Controlled Fusion* **36**, 171 (1994).
- <sup>7</sup>R. P. Schorn *et al.*, “Radial temperature distributions of C<sup>6+</sup> ions in the TEXTOR edge plasma measured with lithium beam activated charge exchange spectroscopy,” *Nucl. Fusion* **32**, 351 (1992).
- <sup>8</sup>H. Ehmler *et al.*, “Charge-exchange spectroscopy at the W7-AS stellarator employing a high-energy Li beam,” *Plasma Phys. Controlled Fusion* **45**, 53 (2003).
- <sup>9</sup>M. Reich *et al.*, “Lithium beam charge exchange diagnostic for edge ion temperature measurements at the ASDEX Upgrade tokamak,” *Plasma Phys. Controlled Fusion* **46**, 797 (2004).
- <sup>10</sup>S. Zoletnik *et al.*, “Advanced neutral alkali beam diagnostics for applications in fusion research (invited),” *Rev. Sci. Instrum.* **89**, 10D107 (2018).
- <sup>11</sup>G. Anda *et al.*, “Measurement of edge plasma parameters at W7-X using alkali beam emission spectroscopy,” *Fusion Eng. Des.* **146**, 1814–1819 (2019).
- <sup>12</sup>S. Zoletnik *et al.*, “Multi-diagnostic analysis of plasma filaments in the island divertor,” *Plasma Phys. Controlled Fusion* **62**, 014017 (2020).
- <sup>13</sup>B. Csillag *et al.*, “Statistical analysis of plasma filaments in the island divertor of Wendelstein 7-X,” *Nucl. Fusion* **64**, 016017 (2024).
- <sup>14</sup>D. Nagy *et al.*, “Development of the W7-X alkali metal beam diagnostic observation system for OP2,” *J. Nucl. Eng.* **4**, 142–151 (2023).
- <sup>15</sup>R. Olson and A. Salop, “Charge-transfer and impact-ionization cross sections for fully and partially stripped positive ions colliding with atomic hydrogen,” *Phys. Rev. A* **16**, 531–541 (1977).
- <sup>16</sup>K. Tókési and G. Hock, “Versatility of the exit channels in the three-body CTMC method,” *Nucl. Instrum. Methods Phys. Res., Sect. B* **86**, 201–204 (1994).
- <sup>17</sup>J. C. Slater, “Atomic shielding constants,” *Phys. Rev.* **36**, 57–64 (1930).
- <sup>18</sup>T. S. Pedersen *et al.*, “Confirmation of the topology of the Wendelstein 7-X magnetic field to better than 1:100,000,” *Nat. Commun.* **7**, 13493 (2016).
- <sup>19</sup>T. Romba *et al.*, “Evaluation and validation of radial impurity density profiles from CXRS using neutral beam modelling in W7-X,” *Plasma Phys. Controlled Fusion* **65**, 075011 (2023).
- <sup>20</sup>R. P. Schorn *et al.*, “Absolute concentrations of light impurity ions in tokamak discharges measured with lithium-beam-activated charge-exchange spectroscopy,” *Appl. Phys. B: Photophys. Laser Chem.* **52**, 71 (1991).